

Enhanced Performance of a Self-Powered Organic/Inorganic Photodetector by Pyro-Phototronic and Piezo-Phototronic Effects

Wenbo Peng, Xingfu Wang, Ruomeng Yu, Yejing Dai, Haiyang Zou, Aurelia C. Wang, Yongning He, and Zhong Lin Wang*

Self-powered photodetectors (PDs) have long been realized by utilizing photovoltaic effect and their performances can be effectively enhanced by introducing the piezo-phototronic effect. Recently, a novel pyro-phototronic effect is invented as an alternative approach for performance enhancement of self-powered PDs. Here, a self-powered organic/inorganic PD is demonstrated and the influences of externally applied strain on the pyro-phototronic and the photovoltaic effects are thoroughly investigated. Under 325 nm 2.30 mW cm^{-2} UV illumination and at a -0.45% compressive strain, the PD's photocurrent is dramatically enhanced from ≈ 14.5 to ≈ 103 nA by combining the pyro-phototronic and piezo-phototronic effects together, showing a significant improvement of over 600%. Theoretical simulations have been carried out via the finite element method to propose the underlying working mechanism. Moreover, the pyro-phototronic effect can be introduced by applying a -0.45% compressive strain to greatly enhance the PD's response to 442 nm illumination, including photocurrent, rise time, and fall time. This work provides in-depth understandings about the pyro-phototronic and the piezo-phototronic effects on the performances of self-powered PD to light sources with different wavelengths and indicates huge potential of these two effects in optoelectronic devices.

A photodetector (PD) is one of the main building blocks of sensors network and Internet of Things, and therefore has attracted tremendous attention for the development of high-performance PDs. Generally, the PDs are fabricated as a metal–semiconductor–metal structure,^[1–4] a Schottky junction,^[5–8] or

a p–n junction,^[9–11] in which the externally applied bias voltage is necessary for achieving high sensitivity, high responsivity, and fast detection speed. In recent years, self-powered PDs have been demonstrated through integrating the PDs with external power sources such as piezoelectric and/or triboelectric nanogenerators to realize a self-powered photodetection system.^[12–15] Besides, the photovoltaic effect can also be utilized to achieve self-powered photodetection.^[16–20] Compared to the integration of PDs with external power sources, the photovoltaic effect is a phenomenon naturally existed in semiconductor junction-based devices,^[21] making the self-powered PDs facile-manufactured and cost-effective.

Current photodetection technologies primarily rely on separate photoconductive semiconductor materials with certain band gaps corresponding to distinct spectral ranges, such as silicon for infrared light,^[10,22,23] low band gap 2D semiconductors for visible light,^[24–26] and gallium nitride (GaN) and zinc oxide (ZnO)

for ultraviolet (UV) light.^[2–4] Among these materials, ZnO has become one prior candidate for fabricating UV PDs due to its wide band gap of 3.37 eV, high exciton binding energy of 60 meV at room temperature, and environmental friendly characteristic.^[27–29] Additionally, wurtzite structured ZnO has piezoelectric effect due to its noncentral-symmetric crystal structure. Piezoelectric polarization charges can be produced by externally applied strains to modulate/tune the charge carriers' generation, separation, transportation, and recombination at the metal/ZnO interface through modifying the Schottky barrier properties, which are able to enhance the ZnO-based PDs' performances and known as the piezo-phototronic effect.^[3,30–33] Moreover, recently a novel working mechanism, called pyro-phototronic effect, is proposed by utilizing light-self-induced pyroelectric effect in ZnO to significantly improve the perovskite/ZnO and the Si/ZnO heterojunction UV PDs' performances.^[34–36] As pyroelectric and piezoelectric effects are both based on the polarization charges generated in ZnO semiconductor material, it is expected that the pyro-phototronic and piezo-phototronic effects can be coupled for further improvement of ZnO-based UV PDs' performances.

Dr. W. Peng, Prof. Y. He
School of Electronic and Information Engineering
Xi'an Jiaotong University
Xi'an 710049, China

Dr. W. Peng, X. Wang, Dr. R. Yu, Prof. Y. Dai, H. Zou,
A. C. Wang, Prof. Z. L. Wang
School of Materials Science and Engineering
Georgia Institute of Technology
Atlanta, GA 30332, USA
E-mail: zhong.wang@mse.gatech.edu

Prof. Z. L. Wang
Beijing Institute of Nanoenergy and Nanosystems
Chinese Academy of Sciences
Beijing 100083, China

DOI: 10.1002/adma.201606698

In this work, a self-powered ZnO-based organic/inorganic PD is prepared and its pyro-phototronic and piezo-phototronic effects are carefully and systematically investigated by varying the power density of 325 nm UV laser and the externally applied strain over a wide range. At a power density of 2.30 mW cm^{-2} , the photocurrent can be improved by $\approx 350\%$ via the pyro-phototronic effect. Further, by introducing a -0.45% compressive strain to the PD, the enhancement of photocurrent can be increased to over 600%. Theoretical simulations are carried out to study the effects of piezoelectric polarization charges produced by externally applied strain on the energy band diagram as well as the pyro-phototronic effect, for thoroughly analyzing the coupling between pyro-phototronic and piezo-phototronic effects. Moreover, the pyro-phototronic effect can also be effectively introduced by applying a -0.45% compressive strain to greatly improve the PD's responses to 442 nm laser. This work provides in-depth understandings about the pyro-phototronic and piezo-phototronic effects on the

performances of self-powered PD to light sources with different wavelengths and indicates huge potential of these two effects in optoelectronic devices, such as broadband PDs, ultrafast photo-detection, and radiation detection.

The structure of the self-powered organic/inorganic PD is schematically illustrated in Figure 1a. First, an $\approx 100 \text{ nm}$ thick ZnO seed layer is deposited on flexible indium tin oxide (ITO)/polyethylene terephthalate (PET) substrate by radio frequency magnetron sputtering. Then, ZnO nanowire array is synthesized via a low-temperature hydrothermal method, followed by spin-coating a highly conductive p-type poly(3,4-ethylenedioxythiophene)-poly(styrene sulfonate) (PEDOT:PSS) layer to form the PEDOT:PSS/ZnO organic/inorganic heterojunction. Finally, a silver (Ag) layer is deposited on the PEDOT:PSS layer as the top electrode. The detailed fabrication process and measurement setups are found in the Experimental Section. The cross-sectional scanning electron microscope (SEM; Hitachi SU8010) image of the PEDOT:PSS/ZnO

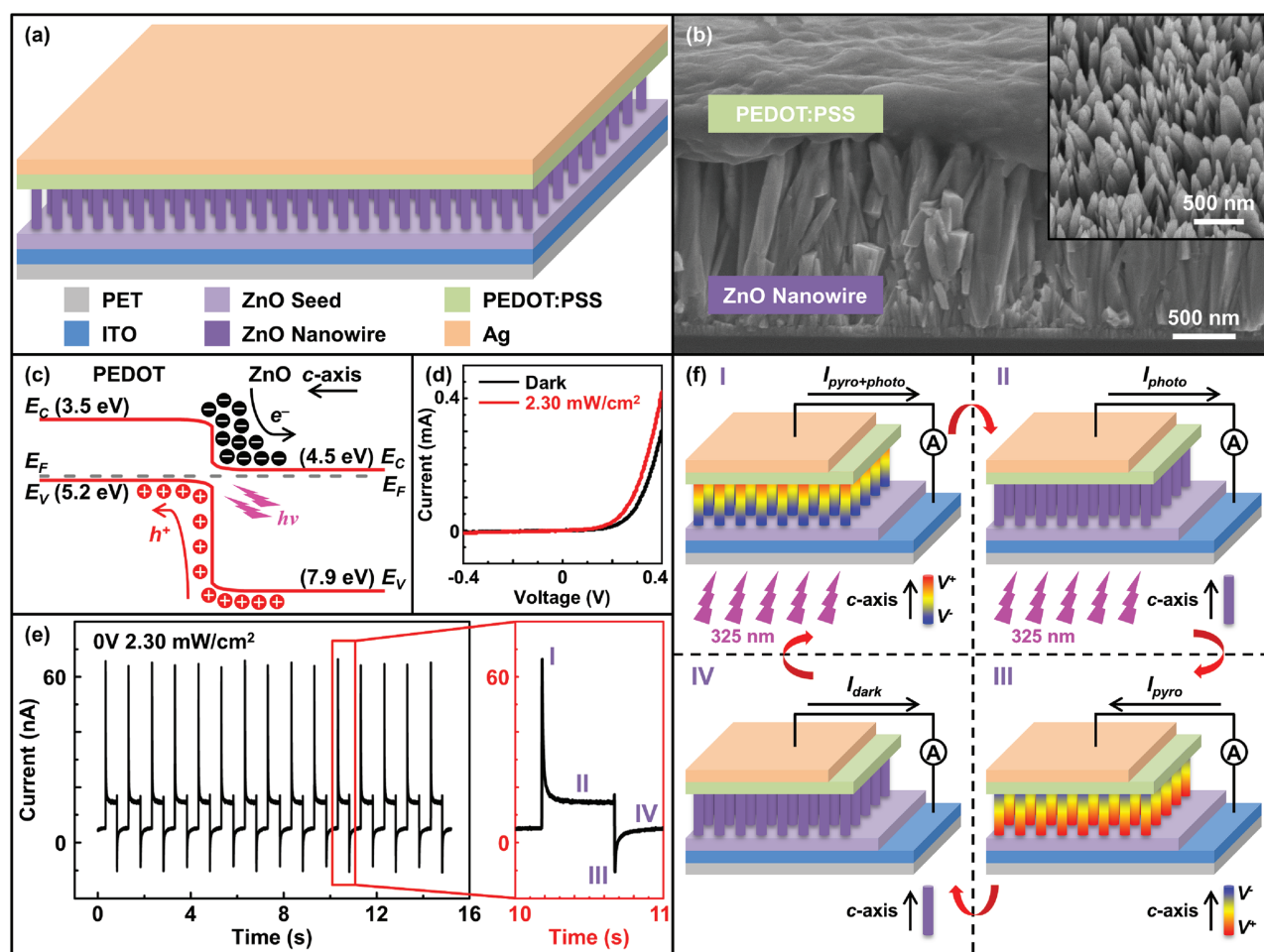


Figure 1. The schematic, characterization, and pyro-phototronic working mechanism of the self-powered PEDOT:PSS/ZnO heterojunction PD. a) Schematic demonstration of the structure of the self-powered PEDOT:PSS/ZnO heterojunction PD. b) Scanning electron microscopy (SEM) image of the PEDOT:PSS/ZnO heterojunction. Inset: Top view SEM image of the ZnO nanowires synthesized via low temperature hydrothermal method. c) Energy band diagram of the PEDOT:PSS/ZnO heterojunction, illustrating the self-powered photodetection working mechanism based on the photovoltaic effect. d) Typical I - V characteristics of the PD under dark and 325 nm 2.30 mW cm^{-2} UV illumination. e) Transient responses of the PD to 325 nm 2.30 mW cm^{-2} UV illumination under zero bias, presenting an obvious four-stage current response behavior. f) Systematical illustration of the fundamental working mechanism of a complete pyro-phototronic effect induced transient current response period to UV illumination.

heterojunction as shown in Figure 1b illustrates a well-formed interface between PEDOT:PSS and ZnO nanowire array, which anticipates outstanding rectification behavior of the PEDOT:PSS/ZnO heterojunction. The inset SEM image in Figure 1b is the top view of the as-synthesized ZnO nanowire array, indicating that the ZnO nanowires have an average radius of ≈ 100 nm and length of ≈ 1.5 μm (Figure 1b). The energy band diagram and the current–voltage (I – V) characteristics of the PEDOT:PSS/ZnO heterojunction under dark and UV illumination conditions are shown in Figure 1c,d. Upon UV illumination, photo-generated electrons and holes are produced at the interface between PEDOT:PSS and ZnO, then separated by the built-in electric field induced by the PEDOT:PSS/ZnO heterojunction, and finally collected by the ITO and Ag electrodes, respectively, forming the corresponding photocurrent.

The transient response of the PD to 325 nm 2.30 mW cm^{-2} UV illumination without external bias voltage (0 V) is shown in Figure 1e, presenting an obvious four-stage photocurrent dynamic behavior, which is caused by the recently invented pyro-phototronic effect.^[34–36] A complete pyro-phototronic effect-induced four-stage photocurrent dynamic behavior is systematically illustrated in Figure 1f. At first, the PD is under the initial dark condition and its current is therefore the dark current I_{dark} . When the UV laser illuminates the PD, the UV photons are absorbed by the ZnO nanowires, leading to the generation of photo-generated electrons and holes and a transient temperature increase of the ZnO nanowires simultaneously. The photo-generated electrons and holes are separated and collected by the ITO and Ag electrodes, respectively, producing the photovoltaic effect induced photocurrent I_{photo} . Meanwhile, the transient temperature increase of the ZnO nanowires due to the UV illumination generates pyroelectric polarization potentials (pyro-potentials) across the ZnO nanowires due to the ZnO material's pyroelectric effect.^[37–40] According to the $+c$ -axis of the ZnO nanowires, positive and negative pyro-potentials occur at the PEDOT:PSS side and the ITO electrode side, respectively, which are in alignment with I_{photo} and hence improve the photocurrent from I_{photo} to a spike $I_{\text{pyro+photo}}$ (Figure 1f, top left panel, stage I). While the PD is under sustained UV illumination, the temperature of the ZnO nanowires keeps almost unchanged because of the weak heating capability of UV laser and no temperature variation is observed in ZnO nanowires, resulting in the disappearance of the pyroelectric effect as well as the pyro-potentials in ZnO nanowires. Consequently, the photocurrent gradually decreases from the spike $I_{\text{pyro+photo}}$ back to a plateau I_{photo} (Figure 1f, top right panel, stage II). When the PD is under dark condition again, a transient temperature decrease of the ZnO nanowires occurs due to the absence of UV illumination, which leads to the opposite distribution of pyro-potentials across the ZnO nanowires with positive and negative pyro-potentials locating at the ITO electrode side and the PEDOT:PSS side, respectively. As a result, a reverse current spike I_{pyro} is produced (Figure 1f, bottom right panel, stage III). While the PD is under sustained dark condition, the temperature of the ZnO nanowires keeps constant and the opposite pyro-potentials across the ZnO nanowires vanish. Thus, the current recovers from the reverse spike I_{pyro} to the initial dark current I_{dark} (Figure 1f, bottom left panel, stage IV).

According to the analysis and discussion above, the pyro-phototronic effect here is defined as the modulation of photo-induced carriers' generation, transportation, and recombination in PEDOT:PSS/ZnO heterojunction through the light-induced pyroelectric potential across the ZnO. More specifically, the pyroelectric potential across the ZnO is utilized to enhance the photovoltaic effect induced photocurrent of the PEDOT:PSS/ZnO heterojunction. The pyroelectric effect is from the ZnO and the photovoltaic effect is from the PEDOT:PSS/ZnO heterojunction, indicating that the PEDOT:PSS layer is the essential element for the introduction of pyro-phototronic effect in PEDOT:PSS/ZnO heterojunction. Moreover, to further confirm this light-induced pyro-phototronic effect, a self-powered p-Si/n-ZnO heterojunction PD has been fabricated and its photoresponse to 150 mW 648 nm laser illumination is measured. From the experimental results shown in Figures S1–S3 (Supporting Information), this p-Si/n-ZnO heterojunction PD exhibits similar four-stage photocurrent dynamic behavior, although ZnO hardly absorbs 648 nm laser illumination, implying that this phenomenon should be attributed to the 648 nm laser illumination-induced heating of the pyroelectric material ZnO. These results confirm that in the PEDOT:PSS/ZnO heterojunction PD, the four-stage photocurrent dynamic behavior is due to the UV light-induced heating of ZnO, i.e., the pyro-phototronic effect. The details about the p-Si/n-ZnO heterojunction PD can be found in the Supporting Information.

The transient responses of the self-powered PEDOT:PSS/ZnO heterojunction PD to 325 nm UV illumination with different power densities ranging from 0.30 to 2.30 mW cm^{-2} under zero bias are systematically investigated and summarized in Figure 2a. Obviously, the pyro-phototronic effect induced four-stage photocurrent dynamic behavior is observed under all the power densities. The $I_{\text{pyro+photo}}$ and I_{photo} under each power density are derived from Figure 2a and plotted in Figure 2b. For all the power density, the PD's photocurrent is enhanced from I_{photo} to $I_{\text{pyro+photo}}$ via the pyro-phototronic effect. Besides, it is noteworthy that the magnitude of the enhancement $E = (I_{\text{pyro+photo}} - I_{\text{photo}})/I_{\text{photo}}$ increases with the power density and achieves a maximum value of $\approx 350\%$ at 2.30 mW cm^{-2} as shown in the inset of Figure 2b, indicating that the pyro-phototronic effect also increases with the power density.^[36] The corresponding responsivity $R_{\text{pyro+photo}}$ and R_{photo} and detectivity $D_{\text{pyro+photo}}$ and D_{photo} under each power density are then calculated and summarized in Figure 2c and Figure S4 (Supporting Information). The average R_{photo} and D_{photo} of all the power densities are nearly ≈ 0.5 mA W^{-1} and $\approx 1 \times 10^9$ Jones, respectively. By introducing the pyro-phototronic effect, the responsivity and detectivity are dramatically enhanced to $R_{\text{pyro+photo}}$ and $D_{\text{pyro+photo}}$ with maximum values of almost ≈ 3.5 mA W^{-1} and $\approx 7.5 \times 10^9$ Jones at 2.30 mW cm^{-2} , respectively, both presenting a maximum enhancement E of over 500% as shown in the insets of Figure 2c and Figure S4 (Supporting Information) and indicating the great potential of pyro-phototronic effect in optoelectronic devices.

The piezo-phototronic effect is then introduced to further modulate the performance of the self-powered PEDOT:PSS/ZnO heterojunction PD. As schematically illustrated in Figure 3a, one end of the PD fabricated on flexible ITO/PET substrate is fixed while the other end is bounded to a

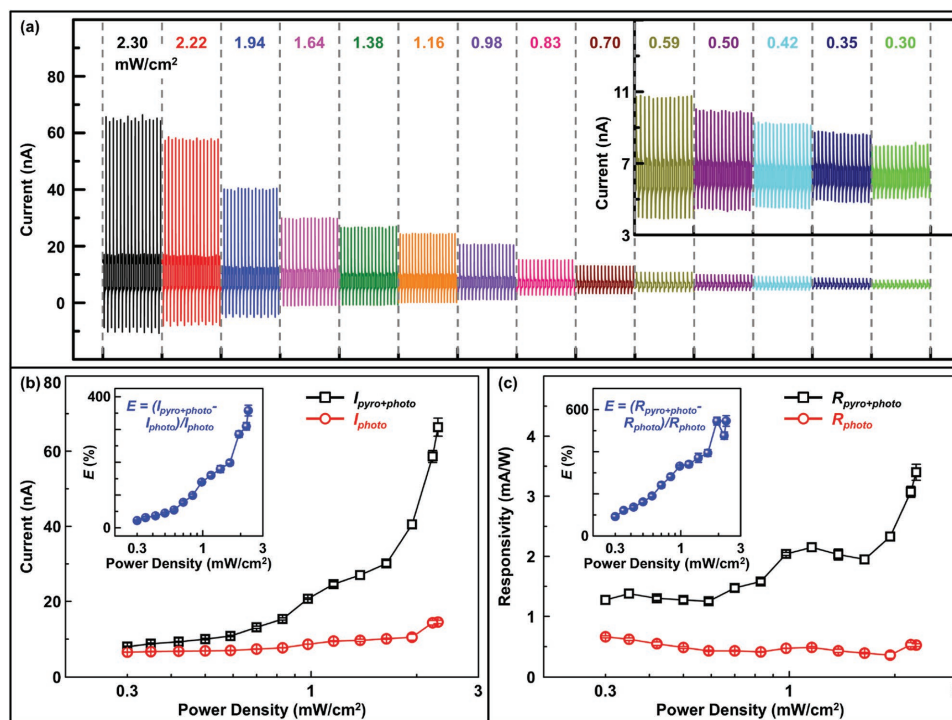


Figure 2. Pyro-phototronic effect enhanced UV detection performances of the self-powered PEDOT:PSS/ZnO heterojunction PD. a) Transient $I-t$ characteristics of the pyro-phototronic effect enhanced PD under 325 nm UV laser with different power densities from 0.30 to 2.30 mW cm^{-2} . Inset: The enlarged $I-t$ characteristics under the corresponding UV illumination conditions. b) The pyro-phototronic effect induced $I_{\text{pyro+photo}}$ and the photovoltaic effect induced I_{photo} as a function of the power density. Inset: The calculated enhancement of photocurrent from I_{photo} to $I_{\text{pyro+photo}}$ under different power densities, showing the enhancement increases with power density. c) The corresponding $R_{\text{pyro+photo}}$ and R_{photo} as a function of the power density. Inset: The calculated enhancement of responsivity from R_{photo} to $R_{\text{pyro+photo}}$ under different power densities, also showing the enhancement increases with power density.

stationary XYZ linear translation stage (462-XYZ-M, Newport Inc.) for facile application of different tensile or compressive strains. The corresponding externally applied tensile/compressive strains could be approximately calculated through the model sketched in Figures S5–S7 (Supporting Information) and the detailed information is found in the Supporting Information. The influences of the externally applied strains on the charge carrier transport properties of the PEDOT:PSS/ZnO heterojunction, also well-known as the piezotronic effect,^[33,41–43] are first studied and the $I-V$ characteristics of the PD under dark condition and different strains from -0.45% to 0.45% are shown in Figure 3b. Clearly, the current/threshold voltage V_{th} increases/decreases with tensile strain and decreases/increases with compressive strain monotonously. The currents at 0.4 V bias under different strains and the corresponding changes of the barrier height ΔBH are derived, calculated, and plotted in Figure 3c. The details of the derivation and calculation of ΔBH are found in the Supporting Information. The current at 0.4 V bias increases from ≈ 0.1 mA at -0.45% compressive strain to ≈ 0.45 mA at 0.45% tensile strain. Correspondingly, the ΔBH decreases from ≈ 30 meV at -0.45% compressive strain to about -10 meV at 0.45% tensile strain, indicating an effective modulation of the barrier height as well as the charge carrier transport properties of the PEDOT:PSS/ZnO heterojunction through externally applied strains.

Then, the transient responses of the self-powered PEDOT:PSS/ZnO heterojunction PD to 325 nm 2.30 mW cm^{-2} UV illumination under different strains are measured and summarized in Figure 3d, to illustrate the piezo-phototronic effect on both the pyro-phototronic and the photovoltaic effects. Different from the results shown in Figure 3b, both the $I_{\text{pyro+photo}}$ and I_{photo} decrease with tensile strain and increase with compressive strain, representing that the pyro-phototronic and the photovoltaic effects are simultaneously modulated in the same direction. The fundamental working mechanisms of these two opposite modulation by externally applied strains in Figure 3b,d are carefully illustrated by the finite element method (FEM) simulated energy band diagram under different tensile and compressive strains, as shown in Figure 3e,f. The details about the FEM simulation are found in the Supporting Information.

For the tensile strain condition (Figure 3e), according to the experimental setup shown in Figure 3a, the length of PD along the a -axis of the ZnO nanowires increases upon tensile strain and thus the length of the ZnO nanowires along their c -axis decreases, producing positive and negative piezoelectric polarization charges (piezo-charges) at the interfaces of ITO/ZnO and PEDOT:PSS/ZnO heterojunction, respectively. These externally applied tensile strain induced negative piezo-charges attract the holes in the p-type PEDOT:PSS layer moving toward and repel the electrons in the n-type ZnO layer away from the interface of PEDOT:PSS/ZnO heterojunction, leading to an upward

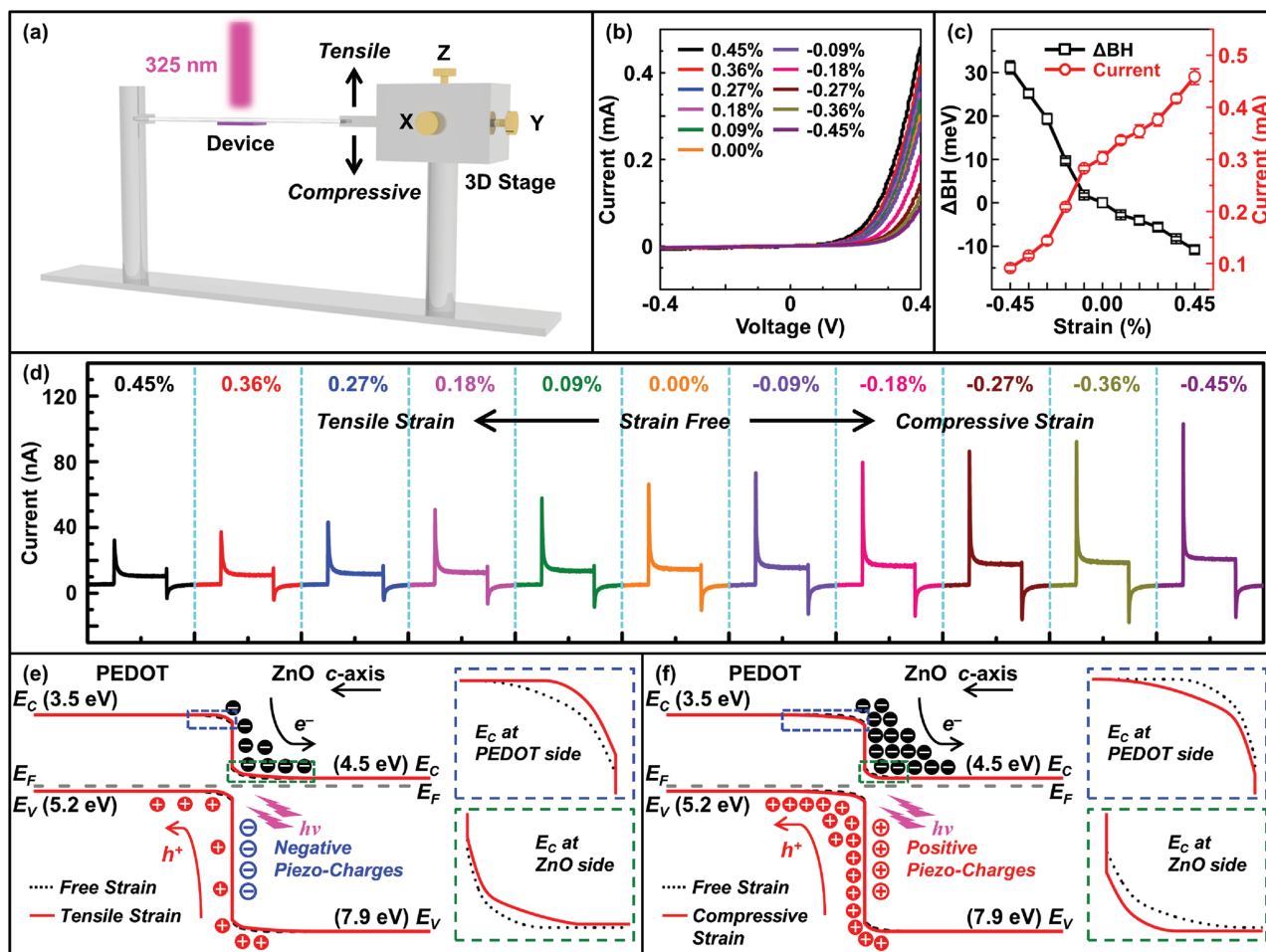


Figure 3. Experimental setup, characterization, and fundamental working mechanisms of the externally applied strains' effects on the self-powered PEDOT:PSS/ZnO heterojunction PD. a) Sketch of the experimental setup showing how tensile and compressive strains are applied. b) Typical I - V characteristics of the PD at dark condition under different strains varying from -0.45% to 0.45% . c) Derived dark current at 0.4 V bias and calculated corresponding barrier height change ΔBH of the PD as a function of the externally applied strain. d) Transient I - t characteristics of the pyro-phototronic effect enhanced PD under 325 nm 2.30 mW cm^{-2} UV illumination with different strains, showing that $I_{\text{pyro+photo}}$ and I_{photo} are reduced/enhanced by externally applied tensile/compressive strain simultaneously. e, f) Theoretical finite element method simulated energy band diagrams of the PEDOT:PSS/ZnO heterojunction under strain free, (e) tensile strain, and (f) compressive strain conditions, carefully illustrating the in-depth physical coupling between the pyro-phototronic and piezo-phototronic effects, which in turn modulate the photocurrents $I_{\text{pyro+photo}}$ and I_{photo} . Insets in (e) and (f): Enlarged conduction band E_C at both PEDOT:PSS and ZnO sides, showing the changes of E_C under (e) tensile and (f) compressive strains.

bending of the energy band diagram of both PEDOT:PSS and ZnO layers. Considering that the PEDOT:PSS is a highly conductive p-type polymer and the ZnO nanowires are synthesized through a low-temperature hydrothermal method, which should not be heavily doped n-type semiconductor material, the magnitude of the upward bending of the energy band diagram at the PEDOT:PSS side is negligible compared to that at the ZnO side,^[21] as illustrated in the insets of Figure 3e. Consequently, the barrier height of the PEDOT:PSS/ZnO heterojunction decreases with tensile strain, leading to the decrease of threshold voltage V_{th} , the increase of current at 0.4 V bias (Figure 3c), and the decrease of photovoltaic effect induced photocurrent I_{photo} as a result of less effective separation and collection of the photo-generated electrons and holes. Moreover, it is noteworthy that the pyro-potential at the interface of PEDOT:PSS/ZnO heterojunction generated by UV illumination is positive, whereas the piezo-charges produced at the

interface by tensile strain are negative, weakening the effective positive pyro-potential and hence reducing the pyro-phototronic effect induced photocurrent $I_{\text{pyro+photo}}$ (Figure 3d).

For the compressive strain condition (Figure 3f), all the results are as opposite as that under tensile strain condition. The piezo-charges produced at the interface of the PEDOT:PSS/ZnO heterojunction are positive and therefore the energy band diagram at both PEDOT:PSS and ZnO sides bend downward. Similarly, the magnitude of the downward bending of the energy band diagram at the PEDOT:PSS side is negligible compared to that at the ZnO side,^[21] resulting in the increase of the barrier height of the PEDOT:PSS/ZnO heterojunction, as shown in the insets of Figure 3f. Hence, the threshold voltage V_{th} increases and the current at 0.4 V bias decreases with compressive strain (Figure 3c). However, more effective separation and collection of the photo-generated electrons and holes are obtained due to higher barrier height of the PEDOT:PSS/ZnO

heterojunction, which improve the photovoltaic effect induced photocurrent I_{photo} . Additionally, the piezo-charges produced by compressive strain and the pyro-potential are both positive at the interface, strengthening the effective positive pyro-potential and thus enhancing the pyro-phototronic effect induced photocurrent $I_{\text{pyro+photo}}$ (Figure 3d). These experimental results and FEM simulated energy band diagram under tensile and compressive strains agree well and for the first time prove that the externally applied strains could not only modify the photovoltaic effect of the PEDOT:PSS/ZnO heterojunction but also modulate its pyro-phototronic effect.

The influences of the externally applied strains on the performance of self-powered PEDOT:PSS/ZnO heterojunction PD to 325 nm UV laser are systematically investigated under different power densities varying from 0.30 to 2.30 mW cm^{-2} and strains ranging from -0.45% to 0.45% . Figure 4a is the $I_{\text{pyro+photo}}$ as a function of the power density under different strains, clearly showing that under each strain condition,

$I_{\text{pyro+photo}}$ increases monotonously with the power density. The corresponding 2D mapping of the $I_{\text{pyro+photo}}$ as functions of the power density and the externally applied strain is plotted in Figure 4b, indicating larger $I_{\text{pyro+photo}}$ could be obtained under stronger power density and smaller strains, with a maximum value of ≈ 103 nA achieved under 325 nm 2.30 mW cm^{-2} UV illumination and -0.45% compressive strain. The relative change of the $I_{\text{pyro+photo}}$ due to the externally applied strains $\Delta I/I_0 = [I(\varepsilon) - I(\varepsilon = 0)]/I(\varepsilon = 0)$ under each strain and power density are calculated and summarized in Figure 4c, indicating that the modulation of $I_{\text{pyro+photo}}$ has an almost linear relationship with the externally applied strain at all the power densities. Under -0.45% compressive strain, a maximum $I_{\text{pyro+photo}}$ enhancement of $\approx 70\%$ and a minimum of $\approx 35\%$ are achieved at 1.94 and 0.98 mW cm^{-2} , respectively. Figure 4d,e shows the responsivity $R_{\text{pyro+photo}}$ as a function of the power density under different strains from -0.45% to 0.45% and the relative change of the $R_{\text{pyro+photo}}$ due to the externally applied strains

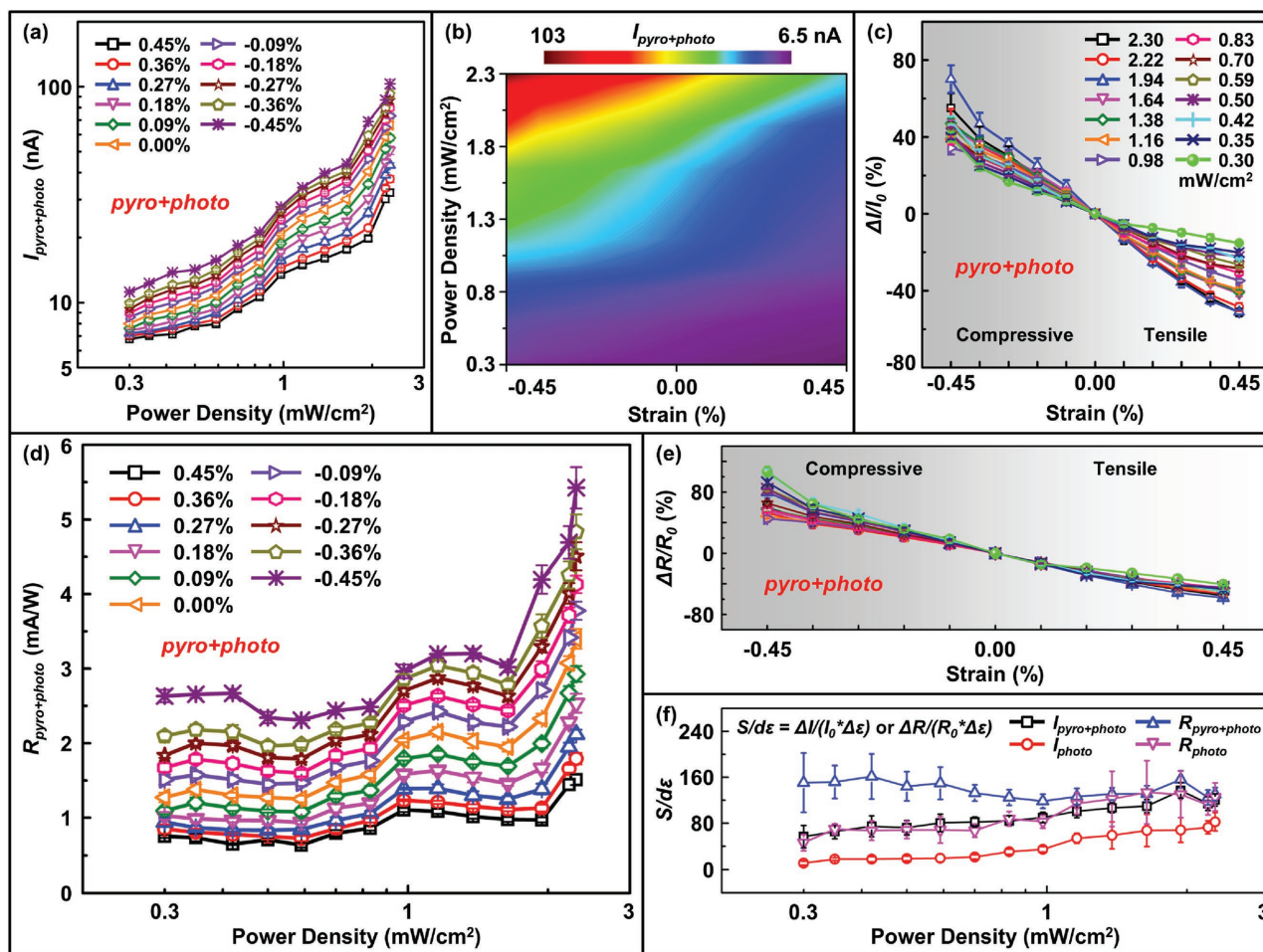


Figure 4. The pyro-phototronic and piezo-phototronic effects on the performances of the self-powered PEDOT:PSS/ZnO heterojunction PD to 325 nm UV laser. a) The $I_{\text{pyro+photo}}$ as a function of power density under different externally applied strains. b) The 2D mapping of the $I_{\text{pyro+photo}}$ as functions of power density and externally applied strain, showing that $I_{\text{pyro+photo}}$ increases monotonously as increasing power density or decreasing externally applied strain. c) The relative change of $I_{\text{pyro+photo}}$, $\Delta I/I_0$, as a function of externally applied strain under different power densities. d) The calculated corresponding $R_{\text{pyro+photo}}$ as a function of power density under different externally applied strains. e) The relative change of $R_{\text{pyro+photo}}$, $\Delta R/R_0$, as a function of externally applied strain under different power densities. f) Parameter $S/d\varepsilon = \Delta I/(I_0 \cdot \Delta\varepsilon)$ or $\Delta R/(R_0 \cdot \Delta\varepsilon)$ as a function of power density for quantitatively evaluating the piezo-phototronic effect on the pyro-phototronic and photovoltaic effects induced photocurrent and responsivity under different power densities.

$\Delta R/R_0 = [R(\varepsilon) - R(\varepsilon = 0)]/R(\varepsilon = 0)$ under each strain and power density, which exhibit similar relationship with the externally applied strain as the $I_{\text{pyro+photo}}$ and the $\Delta I/I_0$. A maximum $R_{\text{pyro+photo}}$ enhancement of over 100% and a minimum of $\approx 40\%$ are achieved at 0.30 and 0.98 mW cm^{-2} , respectively. In addition, the effects of externally applied strain on the photovoltaic effect induced I_{photo} , R_{photo} , $\Delta I/I_0$, and $\Delta R/R_0$ are all derived, calculated, and summarized in Figure S8 (Supporting Information). Similar to $I_{\text{pyro+photo}}$ and $R_{\text{pyro+photo}}$, I_{photo} and R_{photo} could also be effectively modulated by the externally applied strain, with maximum I_{photo} and R_{photo} enhancements of $\approx 45\%$ and $\approx 90\%$ under -0.45% compressive strain.

By defining a parameter $S/\Delta\varepsilon = \Delta I/(I_0 \cdot \Delta\varepsilon)$ or $\Delta R/(R_0 \cdot \Delta\varepsilon)$ as a factor, where S is the relative change of the photocurrent I or the responsivity R due to the externally applied tensile/compressive strains, i.e., $S = \Delta I/I_0 = [I(\varepsilon) - I(\varepsilon = 0)]/I(\varepsilon = 0)$ or $S = \Delta R/R_0 = [R(\varepsilon) - R(\varepsilon = 0)]/R(\varepsilon = 0)$, the influence of the externally applied strain on the enhancement of pyro-phototronic and photovoltaic effects could be evaluated quantitatively, as shown in Figure 4f. For the currents $I_{\text{pyro+photo}}$ and I_{photo} , the externally applied strain's modulation of $I_{\text{pyro+photo}}$ is much larger than that of I_{photo} under all the power densities. For the responsivity $R_{\text{pyro+photo}}$ and R_{photo} , the externally applied strain's modulation of $R_{\text{pyro+photo}}$ keeps almost unchanged with a value of ≈ 160 . While the modulation of R_{photo} increases from ≈ 40 at weak power densities to nearly the same as $R_{\text{pyro+photo}}$ at strong

power densities. Besides, the pyro-phototronic effect induced photocurrent enhancement from I_{photo} to $I_{\text{pyro+photo}}$, defined as $I_{\text{pyro+photo}}/I_{\text{photo}}$, is also evaluated as functions of power density and externally applied strain, as illustrated in Figure S9 (Supporting Information). The $I_{\text{pyro+photo}}/I_{\text{photo}}$ increases as the increase of power density and the decrease of the strain, reaching a maximum value of $\approx 500\%$ at 2.30 mW cm^{-2} and -0.45% compressive strain. In this manner, by combining the pyro-phototronic and piezo-phototronic effects together and considering the photocurrent response of this self-powered PEDOT:PSS/ZnO heterojunction PD to 325 nm 2.30 mW cm^{-2} UV illumination, the photocurrent could be dramatically enhanced from ≈ 14.5 nA (i.e., I_{photo} , without both pyro-phototronic and piezo-phototronic effects) to ≈ 103 nA (i.e., $I_{\text{pyro+photo}}$ under -0.45% compressive strain, with both pyro-phototronic and piezo-phototronic effects), presenting a significant enhancement of over 600%!

The photocurrent response of this self-powered PEDOT:PSS/ZnO heterojunction PD to 442 nm 10 mW cm^{-2} illumination at zero bias under strain free condition is also studied and the result is shown in Figure 5a, similar to that observed in the first work inventing the pyro-phototronic effect.^[34] No pyro-phototronic effect induced spike $I_{\text{pyro+photo}}$ is observed due to the fact that the 442 nm laser is not absorbed by the ZnO nanowires as well as its weak heating capability, which might produces only a very small pyro-potential and it is screened quickly by

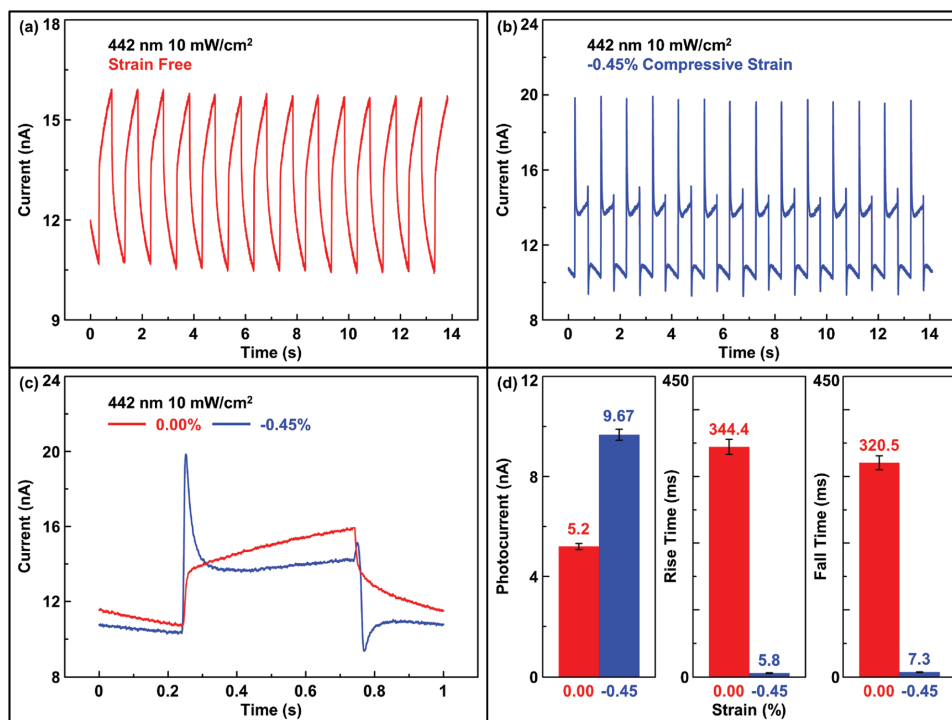


Figure 5. The pyro-phototronic and piezo-phototronic effects on the performances of the self-powered PEDOT:PSS/ZnO heterojunction PD to 442 nm 10 mW cm^{-2} illumination. a) Transient $I-t$ characteristics of the PD under strain free condition, exhibiting no pyro-phototronic effect induced photocurrent spike $I_{\text{pyro+photo}}$. b) Transient $I-t$ characteristics of the PD under a -0.45% compressive strain condition, clearly presenting the pyro-phototronic effect induced photocurrent spike $I_{\text{pyro+photo}}$, which indicates the effective introduction of the pyro-phototronic effect via externally applied compressive strain. c) Enlarged one period transient $I-t$ characteristic of the PD under strain free and -0.45% compressive strain conditions. d) Performances enhancement of the PD to 442 nm 10 mW cm^{-2} illumination by combining the pyro-phototronic and piezo-phototronic effects together, including the absolute photocurrent ($I_{\text{light}}-I_{\text{dark}}$), rise time, and fall time.

the leakage current. Moreover, the current increases/decreases gradually and presents no saturation when the 442 nm laser is periodically turned on/off. However, by applying -0.45% compressive strain to the PD, the pyro-phototronic effect induced spike $I_{\text{pyro+photo}}$ occurs, as positive piezo-charges are generated at the interface of PEDOT:PSS/ZnO heterojunction and thus increase the effective pyro-potential across the ZnO nanowires (Figure 5b). The enlarged transient current response of the PD to 442 nm 10 mW cm^{-2} illumination under both strain free and -0.45% compressive strain conditions is plotted in Figure 5c. The absolute photocurrent ($I_{\text{light}}-I_{\text{dark}}$) and response times including rise time and fall time under two strain conditions, which are defined as the time taken for the current increasing from 10% to 90% and decreasing from 90% to 10% of the maximum photocurrent, respectively, are derived and compared in Figure 5d. The absolute photocurrent is enhanced from ≈ 5.2 to ≈ 9.67 nA, showing an improvement of $\approx 86\%$. More importantly, the rise time and fall time are significantly improved by over 5800% (from ≈ 344.4 to ≈ 5.8 ms) and 4200% (from ≈ 320.5 to 7.3 ms), respectively. These results indicate that even for the light sources with wavelengths not locating in the UV region, the pyro-phototronic effect can still be effectively introduced by externally applied strain to enhance the PD's response (including both absolute photocurrent and response times).

In summary, a self-powered PEDOT:PSS/ZnO organic/inorganic heterojunction PD is demonstrated and both the pyro-phototronic and the piezo-phototronic effects are combined to significantly enhance the PD's performances to 325 and 442 nm lasers. The pyro-phototronic effect is first utilized to improve the photocurrent of PD to 325 nm UV laser for $\approx 350\%$ at 2.30 mW cm^{-2} . The externally applied strains are then introduced to modulate the pyro-phototronic and the photovoltaic effects for further enhancement of the PD's photoresponses. The experimental results indicate that the externally applied strains can effectively modify the photo-generated charge carriers' separation, transportation, and collection efficiency, as well as the pyro-phototronic effect, with a dramatic photocurrent enhancement of over 600% via combining the pyro-phototronic and the piezo-phototronic effects together (from ≈ 14.5 to ≈ 103 nA). Theoretical FEM simulation is conducted to investigate the influences of the piezo-charges produced by externally applied strains on the energy band diagram of the PEDOT:PSS/ZnO heterojunction. With the introduction of piezo-charges, the barrier height of the PEDOT:PSS/ZnO heterojunction and the effective pyro-potential across ZnO nanowires can be controlled by externally applied compressive/tensile strain, which in turn will enhance/reduce the photocurrent. Furthermore, the PD's transient responses to 442 nm laser, including the absolute photocurrent, rise time, and fall time, are greatly improved using externally applied compressive strain to introduce the pyro-phototronic effect. This work provides in-depth understandings about the pyro-phototronic and the piezo-phototronic effects on the performances of self-powered organic/inorganic PD to light sources with different wavelengths and indicates huge potential of these two effects in optoelectronic applications, such as ultrafast photosensing, radiation detection, and biocompatible optoelectronic probes.

Experimental Section

Fabrication Process of Self-Powered PEDOT:PSS/ZnO Heterojunction PDs: The flexible ITO/PET substrate ($60 \Omega \text{ sq}^{-1}$, 7 mil thick) purchased from Sigma-Aldrich was used. ZnO seed layer was deposited by radio frequency magnetron sputtering (PVD 75, Kurt. J. Lesker Company) at the power of 120 W and the chamber pressure of 8 mTorr for 30 min, with the thickness of ≈ 100 nm. The ZnO seed layer coated ITO/PET substrate was then placed into the mixed nutrient solution (25×10^{-3} M zinc nitrate and 12.5×10^{-3} M hexamethylenetetramine) for ZnO nanowires growth via a low-temperature hydrothermal method in a mechanical convection oven (Model Yamato DKN400, Santa Clara, CA, USA) at 95 °C for 1 h. In order to get separated ZnO nanowires, 5 mL ammonium hydroxide (Alfa Aesar) was added per 100 mL mixed nutrient solution. After cooling down the whole system, the sample was washed by ethanol and distilled water, collected, and dried by high purity N_2 gas. Next, a thin layer of PEDOT:PSS (Sigma-Aldrich) was spin-coated on the as-synthesized ZnO nanowires at 3000 rpm with a spin coater (SCS 6800), followed by curing at 120 °C in N_2 atmosphere for 5 min. Then, a thin layer of silver was subsequently sputtered on PEDOT:PSS layer as the top electrode. Testing wires were connected to the top silver and bottom ITO electrodes using a silver paste. A thin layer of Kapton tape was employed to fix the testing wires. Finally, a thin layer of polydimethylsiloxane was used to package the whole device for enhancing its robustness as well as protecting it from possible corrosion or contamination in the environment.

Optical and Electrical Measurements: The electric signals of the device were measured and recorded by a customized computer-controlled measurement system with a function generator (Model No. DS345, Stanford Research Systems, Inc.) and a low-noise current preamplifier (Model No. SR570, Stanford Research Systems, Inc.) in conjunction with a GPIB controller (GPIB-USB-US, NI 488.2). The optical input stimuli were provided by a He-Cd dual-color laser (wavelengths of 325 and 442 nm, Model No. K157511-G, Kimmon Koha Co, Ltd.). A continuously variable filter was used to control the light intensity, which was measured using a thermopile powermeter (Newport 818 P-001-12).

Supporting Information

Supporting Information is available from the Wiley Online Library or from the author.

Acknowledgements

This research was supported by the U.S. Department of Energy, Office of Basic Energy Sciences (Grant No. DEFG02-07ER46394). W.P. would like to acknowledge the support from the China Scholarship Council (CSC).

Keywords

piezo-phototronic effect, pyro-phototronic effect, photodetectors, ZnO

Received: December 11, 2016

Revised: January 24, 2017

Published online:

- [1] Q. S. Guo, A. Pospischil, M. Bhuiyan, H. Jiang, H. Tian, D. Farmer, B. C. Deng, C. Li, S. J. Han, H. Wang, Q. F. Xia, T. P. Ma, T. Mueller, F. N. Xia, *Nano Lett.* **2016**, *16*, 4648.
- [2] C. Soci, A. Zhang, B. Xiang, S. A. Dayeh, D. P. R. Aplin, J. Park, X. Y. Bao, Y. H. Lo, D. Wang, *Nano Lett.* **2007**, *7*, 1003.

- [3] Y. Liu, Q. Yang, Y. Zhang, Z. Y. Yang, Z. L. Wang, *Adv. Mater.* **2012**, *24*, 1410.
- [4] S. W. Seo, K. K. Lee, S. B. Kang, S. Huang, W. A. Doolittle, N. M. Jokerst, A. S. Brown, *Appl. Phys. Lett.* **2001**, *79*, 1372.
- [5] I. Goykhman, U. Sassi, B. Desiatov, N. Mazurski, S. Milana, D. de Fazio, A. Eiden, J. Khurgin, J. Shappir, U. Levy, A. C. Ferrari, *Nano Lett.* **2016**, *16*, 3005.
- [6] T. Yu, F. Wang, Y. Xu, L. L. Ma, X. D. Pi, D. R. Yang, *Adv. Mater.* **2016**, *28*, 4912.
- [7] Y. Fan, Y. Q. Zhou, X. C. Wang, H. J. Tan, Y. M. Rong, J. H. Warner, *Adv. Opt. Mater.* **2016**, *4*, 1573.
- [8] J. S. Miao, S. M. Zhang, L. Cai, C. Wang, *Adv. Electron. Mater.* **2016**, *2*, 1500346.
- [9] B. N. Pal, I. Robel, A. Mohite, R. Laocharoensuk, D. J. Werder, V. I. Klimov, *Adv. Funct. Mater.* **2012**, *22*, 1741.
- [10] L. Wang, J. S. Jie, Z. B. Shao, Q. Zhang, X. H. Zhang, Y. M. Wang, Z. Sun, S. T. Lee, *Adv. Funct. Mater.* **2015**, *25*, 2910.
- [11] Z. N. Wang, R. M. Yu, X. N. Wen, Y. Liu, C. F. Pan, W. Z. Wu, Z. L. Wang, *ACS Nano* **2014**, *8*, 12866.
- [12] Z. H. Lin, G. Cheng, Y. Yang, Y. S. Zhou, S. Lee, Z. L. Wang, *Adv. Funct. Mater.* **2014**, *24*, 2810.
- [13] S. Xu, Y. Qin, C. Xu, Y. G. Wei, R. S. Yang, Z. L. Wang, *Nat. Nanotechnol.* **2010**, *5*, 366.
- [14] L. Su, H. Y. Li, Y. Wang, S. Y. Kuang, Z. L. Wang, G. Zhu, *Nano Energy* **2017**, *31*, 264.
- [15] L. Cheng, Y. Zheng, Q. Xu, Y. Qin, *Adv. Opt. Mater.* **2016**, *5*, 1600623.
- [16] H. Lu, W. Tian, F. R. Cao, Y. L. Ma, B. K. Gu, L. Li, *Adv. Funct. Mater.* **2016**, *26*, 1296.
- [17] H. Y. Chen, P. P. Yu, Z. Z. Zhang, F. Teng, L. X. Zheng, K. Hu, X. S. Fang, *Small* **2016**, *12*, 5809.
- [18] G. H. Li, L. Liu, G. Wu, W. Chen, S. J. Qin, Y. Wang, T. Zhang, *Small* **2016**, *12*, 5019.
- [19] J. C. Yu, X. Chen, Y. Wang, H. Zhou, M. N. Xue, Y. Xu, Z. S. Li, C. Ye, J. Zhang, P. A. V. Aken, P. D. Lund, H. Wang, *J. Mater. Chem. C* **2016**, *4*, 7302.
- [20] C. X. Bao, W. D. Zhu, J. Yang, F. M. Li, S. Gu, Y. R. Q. Wang, T. Yu, J. Zhu, Y. Zhou, Z. G. Zou, *ACS Appl. Mater. Interfaces* **2016**, *8*, 23868.
- [21] S. M. Sze, K. K. Ng, *Physics of Semiconductor Devices*, John Wiley & Sons, Inc., Hoboken, NJ, USA, **2007**.
- [22] Z. Chen, Z. Cheng, J. Wang, X. Wan, C. Shu, H. K. Tsang, H. P. Ho, J.-B. Xu, *Adv. Opt. Mater.* **2015**, *3*, 1207.
- [23] A. Zhang, H. Kim, J. Cheng, Y. H. Lo, *Nano Lett.* **2010**, *10*, 2117.
- [24] R. B. Jacobs-Gedrim, M. Shanmugam, N. Jain, C. A. Durcan, M. T. Murphy, T. M. Murray, R. J. Matyi, R. L. Moore, B. Yu, *ACS Nano* **2014**, *8*, 514.
- [25] M. Buscema, D. J. Groenendijk, S. I. Blanter, G. A. Steele, H. S. J. van der Zant, A. Castellanos-Gomez, *Nano Lett.* **2014**, *14*, 3347.
- [26] M. Massicotte, P. Schmidt, F. Violla, K. G. Schadler, A. Reserbat-Plantey, K. Watanabe, T. Taniguchi, K. J. Tielrooij, F. H. L. Koppens, *Nat. Nanotechnol.* **2016**, *11*, 42.
- [27] C. F. Pan, L. Dong, G. Zhu, S. M. Niu, R. M. Yu, Q. Yang, Y. Liu, Z. L. Wang, *Nat. Photonics* **2013**, *7*, 752.
- [28] R. Yu, C. Pan, J. Chen, G. Zhu, Z. L. Wang, *Adv. Funct. Mater.* **2013**, *23*, 5868.
- [29] R. Yu, C. Pan, Z. L. Wang, *Energy Environ. Sci.* **2013**, *6*, 494.
- [30] Y. Liu, Y. Zhang, Q. Yang, S. Niu, Z. L. Wang, *Nano Energy* **2015**, *14*, 257.
- [31] Q. Yang, W. Wang, S. Xu, Z. L. Wang, *Nano Lett.* **2011**, *11*, 4012.
- [32] Q. Yang, X. Guo, W. Wang, Y. Zhang, S. Xu, D. H. Lien, Z. L. Wang, *ACS Nano* **2010**, *4*, 6285.
- [33] W. Z. Wu, Z. L. Wang, *Nat. Rev. Mater.* **2016**, *1*, 16031.
- [34] Z. N. Wang, R. M. Yu, C. F. Pan, Z. L. Li, J. Yang, F. Yi, Z. L. Wang, *Nat. Commun.* **2015**, *6*, 8401.
- [35] Z. N. Wang, R. M. Yu, X. F. Wang, W. Z. Wu, Z. L. Wang, *Adv. Mater.* **2016**, *28*, 6880.
- [36] W. Peng, R. Yu, X. Wang, Z. Wang, H. Zou, Y. He, Z. L. Wang, *Nano Res.* **2016**, *9*, 3695.
- [37] Y. Yang, W. X. Guo, K. C. Pradel, G. Zhu, Y. S. Zhou, Y. Zhang, Y. F. Hu, L. Lin, Z. L. Wang, *Nano Lett.* **2012**, *12*, 2833.
- [38] T. D. Dao, S. Ishii, T. Yokoyama, T. Sawada, R. P. Sugavaneshwar, K. Chen, Y. Wada, T. Nabatame, T. Nagao, *ACS Photonics* **2016**, *3*, 1271.
- [39] C. C. Hsiao, S. Y. Yu, *Sensors* **2012**, *12*, 17007.
- [40] C. C. Hsiao, K. Y. Huang, Y. C. Hu, *Sensors* **2008**, *8*, 185.
- [41] W. Z. Wu, X. N. Wen, Z. L. Wang, *Science* **2013**, *340*, 952.
- [42] W. Z. Wu, Z. L. Wang, *Nano Lett.* **2011**, *11*, 2779.
- [43] R. M. Yu, X. F. Wang, W. B. Peng, W. Z. Wu, Y. Ding, S. T. Li, Z. L. Wang, *ACS Nano* **2015**, *9*, 9822.